Materials Today Communications 46 (2025) 112463

Contents lists available at ScienceDirect

Materials Today Communications

journal homepage: www.elsevier.com/locate/mtcomm

Extract a directionally-dependent effective capillary radius in porous membranes for wicking prediction in lateral flow assays

Willfried Kunz [a,b,*], Alexander Spreinat [c,e], Christian H. Maack [e], Andrea Ernst [e], Jennifer Niessner [f], Britta Nestler [a,b,d]

[a] Institute of Digital Materials Science, Karlsruhe University of Applied Sciences, Moltkestraße 30, 76133 Karlsruhe, Germany
[b] Institute for Applied Materials - Microstructure Modelling and Simulation, Karlsruhe Institute of Technology (KIT), Strasse am Forum 7, 76131 Karlsruhe, Germany
[c] Leibniz University Hannover, Institute of Technical Chemistry, Callinstraße 5, 30167 Hannover, Germany
[d] Institute of Nanotechnology, Karlsruhe Institute of Technology (KIT), Hermann-von-Helmholtz-Platz 1, 76344 Eggenstein-Leopoldshafen, Germany
[e] Sartorius Stedim Biotech GmbH, August-Spindler-Strasse 11, 37079 Goettingen, Germany
[f] Institute of Flow in Additively Manufactured Porous Media (ISAPS), Heilbronn University of Applied Sciences, Max–Planck-Str. 39, 74081 Heilbronn, Germany

ARTICLE INFO

Keywords:
Paper-based microfluidics
Lateral flow assay
Porous structure
Effective capillary radius
Wicking
Phase-field

ABSTRACT

This study introduces a computational framework for determining a directionally-dependent effective pore radius in porous membranes, enabling precise predictions of capillary-driven wicking behavior, particularly in lateral flow assays (LFAs), a type of medical rapid test widely used for point-of-care testing. By utilizing digital twins generated from 3D high-resolution imaging techniques like confocal laser scanning microscopy and computed tomography, the structural properties of porous polymeric membranes are examined at the pore scale. The primary focus of this work is the determination of the effective pore radius, a critical parameter for accurately modeling capillary-driven wicking behavior. To achieve this, a phase-field approach is employed to simulate two-phase imbibition processes, allowing for the precise derivation of the effective pore radius while explicitly accounting for directional anisotropy. These parameters are then incorporated into a macroscopic Darcy-based wicking model to forecast wicking behavior at the application scale. Experimental validation demonstrates that this methodology provides accurate predictions of wicking behavior across various membrane samples, while also accounting for directionally-dependent wicking effects. This targeted approach enables a deeper understanding of the relationship between pore-scale structure and macroscopic fluid flow. Additionally, the method demonstrates its versatility by allowing the extraction of wetting properties, such as surface energy and contact angle. This computational approach serves as a cost-effective alternative to experimental analyses and offers valuable insights for optimizing porous membrane designs for LFAs and other applications that require precise control of liquid flow.

1. Introduction

Wicking, the capillary-driven imbibition of a wetting fluid into a porous microstructure [1], is a key process underpinning the functionality of many industrial and medical applications, including lateral flow assays (LFAs). LFAs, such as the widely used COVID-19 rapid tests during the pandemic, highlight the benefits of point-of-care testing (POCT) devices. These devices have experienced increasing demand due to their ease of use, cost-effectiveness, and suitability for rapid diagnostics. The operation of LFAs is based on the capillary-driven flow (wicking) of test liquids, such as urine or saliva, through open-pored, highly porous polymeric membranes (PPMs) made of nitrocellulose (NC). These membranes not only efficiently guide the liquid sample to the test line but also act as self-contained microfluidic pumps, directing both the sample and detector particles toward the detection zone, where the test result is displayed through a color signal. Despite the widespread use and large-scale production of LFAs, the interplay between liquid flow and the microstructural properties of the integrated porous membranes is not yet fully understood. To enhance test design, it is crucial to characterize the microstructural features of these membranes at the pore scale (micrometer level) and investigate their influence on the macroscopic wicking behavior (centimeter level). Understanding these interactions will facilitate the optimization of LFAs,

* Corresponding author at: Institute of Digital Materials Science, Karlsruhe University of Applied Sciences, Moltkestraße 30, 76133 Karlsruhe, Germany.
E-mail addresses: willfried.kunz@h-ka.de (W. Kunz), andrea.ernst@sartorius.com (A. Ernst), jennifer.niessner@hs-heilbronn.de (J. Niessner), britta.nestler@kit.edu (B. Nestler).

https://doi.org/10.1016/j.mtcomm.2025.112463
Received 5 February 2025; Received in revised form 21 March 2025; Accepted 6 April 2025
Available online 19 April 2025

enhancing their performance and reliability while making a significant contribution to global health [2].

There are various models for describing the macroscopic wicking behavior in porous microstructures. The two most widely used approaches rely on the Lucas–Washburn equation and Darcy's law, which are thoroughly covered in the scientific literature [3–5]. These approaches share the requirement for effective structural parameters to predict the wicking process. They employ a bottom-up approach, wherein information is propagated from the smallest relevant scale to successively larger scales [6], utilizing effective parameters to bridge the scale gap. To effectively apply these approaches, precise determination of effective parameters is essential. These parameters, such as porosity and permeability, can either be determined through experimental investigations or derived as fitting parameters [7]. Both scenarios require expensive experimental studies. In contrast to traditional methods that rely on the experimental determination of effective parameters, a computational approach can be adopted by utilizing algorithmic and numerical data analysis tools. A method proposed by Altschuh et al. [8] utilizes a digital twin of the porous microstructure to extract structural parameters, enabling the prediction of macroscopic wicking behavior. Digital twins are virtual representations of real-world objects, generated by processing data obtained from 3D imaging techniques. A commonly used 3D imaging method for porous media is high-resolution computed tomography (CT) [8–10]. During CT scans, the microstructure is illuminated layer-by-layer with a high-energy X-ray beam from various angles. The resulting data is then reconstructed to create a 3D digital representation of the microstructure. Further, confocal microscopy can be used to reconstruct the 3D microstructure under certain conditions. For instance, using an immersion oil with a refractive index matching that of the nitrocellulose makes the membrane transparent. This enables the detection of fluorescent particles within the depth of the sample through a scanning process [11,12]. By directly analyzing a digital twin of the microstructure, it bypasses the need for potentially time-consuming and expensive experimental measurements of effective parameters. Additionally, digital twins can provide detailed information about the pore space geometry, which can be crucial for accurately predicting complex wicking behavior.

Specifically, for modeling the capillary-driven wicking process, the representation of the capillary pressure Δp_c is of central importance. As the driving mechanism for wicking, this pressure is usually modeled using the Young–Laplace equation [13], which describes capillary effects at the pore scale—that is, at the level of individual pores within the porous structure. This describes the pressure difference acting on the interface between two immiscible fluids in contact with a solid, as follows:

$$\Delta p_c = \frac{2\gamma_{lg}\cos(\theta_e)}{r_c}. \tag{1}$$

The surface energy between the interacting fluids is denoted by γ_{lg}, while θ_e represents the equilibrium contact angle between the fluid–fluid interface and the solid. Thereby, the capillary pore radius r_c plays a pivotal role in modeling this pressure. For closed axisymmetric capillaries, an analytical connection between r_c and the geometric pore radius can be derived [14]. However, due to the complex pore structure of open-pored, highly porous PPMs, the geometric pore radius r_p is insufficient for an accurate capillary pressure modeling. Furthermore, the flow paths within the porous membranes are not straight and parallel but exhibit a tortuous nature. Therefore, a distinction must be made between the geometric radius and the effective capillary pore radius in complex porous structures [15]. Experiments [16] as well as simulations [8,10] have shown that for such structures, the ratio between the geometric and an effective capillary pore radius can be mapped by a correction factor $F(r_l, r_p)$, which is dependent on the mean ligament radius r_l and the geometric pore radius r_p

$$r_c = F(r_l, r_p)\cdot r_p. \tag{2}$$

Thereby, Altschuh et al. [8] derived the correction factor presented in Eq. (2) by simulating the capillary rise in simplified structures. This approach for calculating a correction factor showed good agreement with experimental wicking profiles when comparing the prediction of the wicking behavior based on a digital twin in PPMs. However, this approach fails to account for the directional dependence of the capillary pressure within PPMs. To overcome this limitation, a method is proposed to determine an effective capillary radius r_{eff} through two-phase imbibition simulations based on a phase-field approach, directly applied to a digital twin of the porous structure. By varying boundary conditions, directional dependence can be explicitly incorporated. The resulting effective parameters will be validated by comparing simulations of macroscopic wicking behavior with experimental data. Additionally, an application example of the proposed method will be demonstrated by estimating the wetting properties, γ_{lg} and θ, through an experimental wicking analysis conducted in a PPM.

The presented determination of a directionally-dependent effective capillary radius is based on the PhD Thesis [12], which is written in German. To reach a broader audience, some results of the work are summarized and recapitulated in this article.

2. Materials and methods

2.1. Mathematical modeling

In the following subsection, the phase-field approach for simulating two-phase fluid flow at the pore scale will first be explained. Subsequently, the mathematical model for predicting wicking behavior at the macroscopic scale will be presented.

2.1.1. Two-phase phase-field approach

The behavior of wetting in porous media can be understood from both a mechanical and an energetic perspective. Mechanically, the capillary force, which is the pressure drop across a curved surface, causes the fluid to be drawn into the pore space. This process, described at the pore scale in terms of capillary pressure Δp_c, can be understood as the driving mechanism for imbibition or wetting in porous media. Energetically, spontaneous wetting is driven by the difference in total surface energies, $\Delta\gamma = \gamma_{sg} - \gamma_{sl}$, where γ_{sg} and γ_{sl} denote the interfaces between a solid substrate (s) and the gas (g) and liquid (l) phases, respectively. When the surface energy difference $\Delta\gamma > 0$ is positive, the system minimizes its total free energy by allowing the liquid to wet the substrate. These two perspectives are interconnected by Young's equation, $\gamma_{lg}\cos(\theta_e) = \gamma_{sg} - \gamma_{sl}$, which relates the difference in total surface energies $\Delta\gamma$ to the equilibrium contact angle θ_e and the surface energy γ_{lg} between the liquid and the gas phase [17].

The investigation of wetting dynamics and the development of free surface curvatures in open-pored cross sections can be comprehensively conducted using a two-phase phase-field method. This approach utilizes a Ginzburg–Landau free energy density functional [18,19] as its foundation. In this method, two order parameters, $\phi_g(\mathbf{x}, t)$ for gas and $\phi_l(\mathbf{x}, t)$ for liquid, are employed. These parameters range from 1 within the liquid phase to 0 outside it. Given the constraint $\phi_l(\mathbf{x}, t) + \phi_g(\mathbf{x}, t) = 1$, a single order parameter $\phi(\mathbf{x}, t) = \phi_l(\mathbf{x}, t) = 1 - \phi_g(\mathbf{x}, t)$ suffices to describe the system.

In the following phase-field model [20], a diffuse interface is created between the gas and liquid phases, with the order parameter smoothly transitioning from $\phi(\mathbf{x}, t) = 1$ in the liquid to $\phi(\mathbf{x}, t) = 0$ in the gas, enabling the interface's position to be monitored over time and space. Furthermore, the model incorporates a wetting boundary condition [20] to account for the surface energy differences $\Delta\gamma$ on the substrate, which is essential for describing wetting behavior. This comprehensive two-phase phase-field approach is encapsulated as follows:

$$F(\phi) = \int_\Omega \left(\epsilon\gamma_{lg}|\nabla\phi|^2 + \frac{1}{\epsilon}w(\phi) + f_g(\phi)\right) \mathrm{d}\Omega + \int_{\partial_s\Omega} f_w(\phi)\, \mathrm{d}S. \tag{3}$$

In this scenario, Ω signifies the spatial domain, and ϵ is a parameter that defines the thickness of the diffuse interface. The term $\gamma_{lg}|\nabla\phi|^2$ represents the gradient energy density, while $w(\phi)$ is the multi-obstacle potential, both of which contribute to the free surface energy of the liquid–gas interface. The expression $f_g(\phi) = \mathbf{g}\cdot\mathbf{x}\rho I(\phi)$ captures the hydrostatic pressure, which varies with the position of the interface in space $\mathbf{x}$, the density ρ and the gravitational force $\mathbf{g}$. The function $I(\phi) = \phi^3(6\phi^2 - 15\phi + 10)$ interpolates values across the diffuse interface [20]. This specific formulation ensures smooth transitions between phases while maintaining numerical stability. Notably, the first derivative of $I(\phi)$ vanishes in the bulk phases ($\phi = 0$ and $\phi = 1$), which prevents artificial forces at equilibrium and preserves the physical consistency of the phase-field representation.

To model the energy effects on the substrate surface $\partial_s\Omega$, the energy formulation $f_w(\phi)$ is applied, described as follows:

$$f_w(\phi) = \gamma_{gs} + (\gamma_{ls} - \gamma_{gs})I(\phi). \tag{4}$$

Through a straightforward analysis of the liquid–gas interface and the substrate surface, it is evident that the imposed wetting boundary condition adheres to Young's law [20]. The evolution of the interface, dependent on both time and space, is derived by minimizing the free energy functional presented in Eq. (3) using variational calculus. This minimization process leads to partial differential equations known as the Allen–Cahn equations, which can be expressed as follows:

$$\tau\epsilon\frac{\partial\phi}{\partial t} = 2\epsilon\gamma_{lg}\Delta\phi - \frac{1}{\epsilon}\frac{\partial w}{\partial\phi}(\phi) - \frac{\partial f_g}{\partial\phi}(\phi), \quad \text{in} \quad \Omega, \tag{5}$$

where τ represents a relaxation parameter, which describes the mobility of the diffuse interface. The wetting boundary condition reads as

$$-2\epsilon\gamma_{lg}\nabla\phi\cdot\mathbf{n} + (\gamma_{gs} - \gamma_{ls})\frac{\partial I}{\partial\phi} = 0 \quad \text{on} \quad \partial_s\Omega. \tag{6}$$

Here, the normal vector to the substrate surface $\partial_s\Omega$ is denoted as $\mathbf{n}$.

2.1.2. Macroscopic flow model for wicking processes

The primary reason for employing macroscopic flow models is to provide straightforward analytical equations for complex flow problems. Additionally, these models are crucial for connecting different length scales.

There are three principal methods used to describe the fluid flow, all of which rely on capturing the process by incorporating key effects such as friction, gravity, and capillarity into the momentum balance equation. Given that porous membranes are assumed to be completely wetted and their intricate structure cannot be represented by a simple bundle of aligned capillaries, a model based on Darcy's law is utilized [21]. In this context, the force balance is formulated as follows:

$$\rho\frac{d(h\dot{h})}{dt} + \frac{\varphi}{K}\eta h\dot{h} + \rho g h = \frac{2\gamma_{lg}\cos(\theta_e)}{r_{eff}}. \tag{7}$$

The equation balances inertial forces (first term), viscous friction (second term), and gravitational forces (third term) on the left side against the capillary force (fourth term) on the right side. Fluid properties like dynamic viscosity η and surface energy γ_{lg}, along with the fluid–substrate interaction characterized by the contact angle θ_e, influence these forces. The effective microstructure of the porous medium is captured by the permeability K, porosity φ, and an effective pore radius r_{eff}. This work focuses on understanding the role of the effective pore radius. Characteristic parameters for the imbibition process include the propagation distance h and velocity $\dot{h}$, which are compared with experimental results.

Note that in the current formulation of the model, no distribution of pore sizes or pore network heterogeneity is considered. The model assumes a homogeneous porous medium with a single effective pore radius r_{eff} to describe the capillary dynamics. The effects of pore distribution, such as varying pore sizes and pore connectivity, are not accounted for in this macroscopic approach. However, this limitation will be addressed in future work, where the impact of pore distribution on the wicking behavior will be explored in more detail.

Depending on the relative magnitudes of these forces, some terms in Eq. (7) can be neglected. A common approach to quantify the dominant forces is by estimating the Bond number (Bo), as described in [22]

$$Bo = \frac{\text{Body force}}{\text{Surface energy force}} = \frac{\rho g h_{max} L}{2\gamma_{lg}} \tag{8}$$

and the Weber number (We) [23] with

$$We = \frac{\text{Inertial force}}{\text{Surface energy force}} = \frac{\rho\dot{h}^2 L}{\gamma_{lg}}, \tag{9}$$

where L is the characteristic length scale of the system and h_{max} describes the maximum vertical height of a rising water column. Geometric pore sizes, ranging from 1 µm to 10 µm, are chosen as the characteristic length scale L due to the specific porous polymeric membranes of interest. Furthermore, the experimental setup in this study (detailed in Section 2.4) involves a membrane sample with a maximum vertical height of $h_{max} = 0.04$ m. Assuming a total wicking time of 140 s to fully wet a vertical distance of h_{max}, the resulting mean wicking velocity $\dot{h}$ is approximately $0.286\,\text{mm}\,\text{s}^{-1}$. For clarity, the 140 s wicking time is an average value for the observed membranes, as provided by the manufacturer. Additionally, the chosen liquid (see Section 3.2.2) has a higher density and lower surface energy compared to water. These combined factors lead to a low Weber number ($We \ll 1$), indicating negligible inertial effects. However, the resulting Bond number, $Bo = 0.22$, is not significantly less than 1, suggesting that surface energy forces might not be the sole dominant factor. This implies that neglecting gravitational forces might not be appropriate. Consequently, the governing equation for imbibition in this case should represent a balance between viscous, gravitational, and capillary forces:

$$\frac{\varphi}{K}\eta h\dot{h} + \rho g h = \frac{2\gamma_{lg}\cos(\theta_e)}{r_{eff}}. \tag{10}$$

If the tortuos flow path h_t of the height h is further considered in the viscous term of the momentum balance as described in [24], the following relationship results from Eq. (10):

$$\frac{\varphi}{K}\eta h_t\dot{h}_t + \rho g h = \frac{2\gamma_{lg}\cos(\theta_e)}{r_{eff}}. \tag{11}$$

The tortuos flow path h_t and the propagation distance h are here linked by the tortuosity τ to

$$h_t = \tau h \tag{12}$$

and

$$\dot{h}_t = \tau\dot{h}. \tag{13}$$

For the applied force balance, a fully analytical solution is given in [21] as follows:

$$h(t) = \frac{1}{c}\left[1 + W(-e^{-1-\frac{c^2 t}{b}})\right]. \tag{14}$$

Here, $W(x)$ is the Lambert function and the variables b and c represent two coefficients for the gravity and viscosity terms, respectively [4]. They can be defined as

$$b = \frac{r_{eff}}{2\gamma_{lg}\cos(\theta_e)}\frac{\varphi\eta\tau^2}{K} \tag{15}$$

and

$$c = \frac{r_{eff}}{2\gamma_{lg}\cos(\theta_e)}\rho g. \tag{16}$$

Eqs. (14)–(16) serve as a macroscopic model for predicting wicking behavior in porous structures. Effective structural properties such as

permeability K, porosity φ, tortuosity τ, and effective pore radius r_{eff} are derived from 3D digital twins of porous polymeric membranes. The wetting properties, including viscosity η, contact angle θ_e, and surface energy γ_{lg}, are based on manufacturer specifications.

The macroscopic flow model presented here is primarily applied in the study of wicking processes within porous media, which is of significant interest in a variety of industrial and scientific domains. For instance, this model can be applied to predict the transport of liquids in porous materials such as membranes and filters, which are widely used in fields like water filtration, battery technology, fuel cells, and textile engineering. In these applications, understanding how a liquid propagates through the porous structure is critical for optimizing the performance of the material.

2.2. Generating digital twins of porous polymeric membranes (PPMs)

A method is introduced for constructing digital twins of real membrane structures using advanced imaging techniques. The reconstruction process relies on high-resolution three-dimensional (3D) tomographic scans of actual membranes. Two methods were employed to obtain image data: (i) A membrane structure was directly characterized using confocal laser scanning microscopy (CLSM) to capture its detailed morphology and (ii) data for two additional membrane structures were obtained from the literature [10], where the authors employed computer tomography (nano-CT) for imaging the microstructure. This integration allows to expand the morphological dataset and investigate a broader range of membrane properties.

The investigated PPMs are unsupported and impregnated nitrocellulose membranes for lateral flow assays, produced by the company Sartorius Stedim Biotech GmbH, Göttingen, Germany. Three different membrane samples are investigated: Sample A and B, taken from the literature [10], are of the same membrane type (commercially available as UniSart® CN140) and sample C is based on a non commercially available modification of the membrane type UniSart® CN140. As specified by the manufacturer, the membrane type UniSart® CN140 has a nominal pore size of 8 µm and a thickness of ~135 µm, while the impregnation of the intrinsic surface provokes the hydrophilic wetting behavior.

2.2.1. Microstructure imaging using CLSM

This section describes the preparation process for a membrane sample to enable its microstructure visualization using confocal laser scanning microscopy. For details regarding the imaging procedures employed for the two additional datasets acquired via nano-CT, the reader is referred to the work of Altschuh et al. [8].

Sample preparation was conducted according to the following protocol. First, the membrane sample to be microscoped (dimensions: 1 cm × 0.5 cm) was dried in an oven at 50 °C for at least two hours under ambient pressure. Subsequently, the specific IgG-bound dye (*Goat anti-Mouse IgG (H+L) Cross-Adsorbed Secondary Antibody, Alexa Fluor®555, Invitrogen®*, A21422 from Thermo Fisher) was diluted to a concentration of 40 µg mL^{-1} in adsorption buffer (pH = 8.0, 5 mM borate, 150 mM NaCl, 1% sucrose). The membrane specimen was subsequently incubated in 1 mL of the dye solution for approximately 48 h at 8 °C. Afterwards, the incubated membrane was dried for at least two hours at 50 °C until completely dry. As the final step of sample preparation, the dried membrane was dripped with Zeiss immersion oil *Immersol 518 F*.

For subsequent microscopy, a *Leica TCS SPE* microscope was employed. An excitation wavelength of 555 nm was selected to match the *Alexa Fluor®555* fluorescent dye. To reconstruct the membrane structure, an image resolution of 80 nm/Pixel was consistently used, whereby an image area of 163.84 µm × 163.84 µm was microscoped across the entire membrane thickness of ~135 µm. The preparation and microscopy of the membrane structure were developed and performed by the company *Sartorius Stedim Biotech GmbH*.

2.2.2. Reconstruction of the digital twin

To enable reliable segmentation of the image stack into pore and structural regions, a careful pre-processing of the 8-bit images is required. The aim of this processing is to minimize unwanted artifacts such as intensity gradients along the image stack axis and image noise.

In a first step, each image of the stack was normalized to its maximum gray value. This normalization serves to compensate for intensity gradients, which are commonly observed in confocal laser scanning microscopy, and which correspond to the thickness of the membranes. To further suppress image noise, a Gaussian filter with a fixed standard deviation of $\sigma = 450$ nm was applied according to Altschuh et al. [8,10]. The subsequent segmentation into foreground (structure) and background (pores) requires the definition of a suitable threshold. Although methods as described by Otsu et al. [25] and Huang et al. [26] are widely used, they are less suitable for the CLSM data, which do not exhibit a clear bimodal gray value distribution. Therefore, the following segmentation method described by Ley et al. [11] was chosen. To determine the optimal threshold, an iterative procedure was applied. The threshold was increased step by step, and after each increase, the porosity of the segmented structure was calculated. The threshold that resulted in a porosity closest to the experimentally determined porosity was defined as the final threshold. The experimental porosity was determined using the weighing method as described in [11]. As final step, the segmented image stack is merged to form a 3D voxel structure. A complete computational characterization of the membrane structure obtained by CLSM was performed, encompassing a lateral area of 160 µm × 160 µm and the entire membrane thickness. This comprehensive analysis satisfies the requirements for a representative volume element (RVE) as defined by Altschuh [10] for such membrane types. The two membrane datasets used from the literature [10], obtained via computed tomography, were reconstructed using the same workflow with the exception of the initial intensity filtering step, which was not necessary.

2.3. Computational determination of structure characteristics

Image analysis algorithms are employed to characterize the relevant structural properties based on the full voxel representation of the digital twins. The computational implementation of these algorithms is carried out within the PACE3D [27] framework.

2.3.1. Porosity

Porosity, a crucial structural parameter in membrane science, is often correlated with the material's overall behavior. To quantify porosity φ, the voxel values $I_{\text{b}}(\mathbf{x})$ at positions $\mathbf{x}$, which equal $I_{\text{b}}(\mathbf{x}) = 1$ represent the pore space and are summed across the entire domain.

$$\varphi = \frac{1}{(N_{\text{x}} \cdot N_{\text{y}} \cdot N_{\text{z}})} \cdot \sum_{i=1}^{N_{\text{x}}} \sum_{j=1}^{N_{\text{y}}} \sum_{k=1}^{N_{\text{z}}} I_{\text{b}}(\mathbf{x}) = \frac{N_{\text{P}}}{N}, \tag{17}$$

where N_{p} is the number of voxels in the pore space, N_{x}, N_{y}, N_{z} are the numbers of voxels along the x-, y-, and z-direction, and N is the total number of voxels in the domain.

2.3.2. Tortuosity

A simulated calculation of the directionally-dependent tortuosity is performed by solving for the electric potential Φ within the pore space of a porous structure. The local gradient of the potential field, $\nabla\Phi$, within the pore space is determined using the following Laplace equation:

$$\nabla \cdot (-\sigma_{\text{P}} \nabla \Phi) = 0. \tag{18}$$

The intrinsic conductivity σ_{P} is assumed to be given, and as an boundary condition, a potential difference of $\Delta\,\Phi = 1.0$ V is set at two opposite domain boundaries. At the interface between the pore space and the structure, a homogeneous Neumann boundary condition is defined,

Table 1
Effective structural properties of the three observed porous NC membranes, including the porosity φ and the directionally dependent properties: tortuosity τ, permeability K and the effective pore radius r_{eff} (calculated using the method outlined in Section 3.1).

Sample	φ (–)	τ_x (–)	τ_y (–)	K_{xx} (10^{-13} m^2)	K_{yy} (10^{-13} m^2)	$r_{\text{eff},x}$ (µm)	$r_{\text{eff},y}$ (µm)
A	0.82	1.198	1.214	7.78	7.30	10.45	11.09
B	0.82	1.211	1.214	6.86	6.45	9.57	9.80
C	0.90	1.119	1.128	23.00	21.71	21.62	23.67

which allows no flux perpendicular to the surface. By applying Ohm's law to the current I resulting from $\nabla\Phi$, the effective resistance R and thus the effective conductivity σ_{eff} can be determined with

$$\sigma_{\text{eff}} = \frac{I}{\nabla\Phi}\frac{L}{A}\,. \tag{19}$$

Here, L represents the total length of the domain under investigation and A denotes the corresponding cross-sectional area. Utilizing the known porosity φ the tortuosity can be calculated as follows [28]:

$$\tau = \varphi\frac{\sigma_{\text{P}}}{\sigma_{\text{eff}}}. \tag{20}$$

By varying the boundary condition, the tortuosity can be determined for all three spatial directions. The calculations are performed using the simulation environment PACE3D [27]. A validation of the implemented algorithm, which is based on the work of Hoffrogge et al. [29], can be found in [10].

2.3.3. Permeability

As a material property, permeability quantifies the inverse of the resistance of porous materials to the flow of fluids, including both Newtonian and non-Newtonian fluids. In general, the permeability $\mathbf{K}$ is a second rank tensor [30], which is symmetric when the coordinate system is aligned with the principal axes of the tensor. Since wicking is characterized by a single main flow direction, only the mean values in the flow direction are considered, while the corresponding indices in the equation are neglected. To determine the permeability, fluid flow simulations are performed in the pore space by defining a pressure difference ∇p across the considered PPM layer with a thickness s and solving the Stokes equations for the steady-state velocity distribution $\mathbf{v} = (u_{\text{x}},\ u_{\text{y}},\ u_{\text{z}})^T$

$$\eta\nabla^2\mathbf{v} - \nabla p = 0\cdot \tag{21}$$

By applying Darcy's law, the permeability is then calculated as follows:

$$K = \frac{\eta U s}{\Delta p}, \tag{22}$$

where η describes the dynamic viscosity and U denotes the Darcy velocity in the main flow direction (e.g. $U = \varphi\cdot\bar{u}_{\text{x}}$). By varying the pressure boundary conditions Δp, the diagonal elements K_{xx}, K_{yy} und K_{zz} of the permeability tensor $\mathbf{K}$ can be determined. The fluid flow solver is implemented within the simulation environment PACE3D [27]. A validation of the permeability determination methodology is detailed in [31].

All extracted effective structure properties of the three observed membrane samples A, B and C are listed in Table 1. Thereby, only fluid flow along the lateral directions x and y is of interest, as the z-direction represents the membrane thickness.

2.4. Experimental setup for detecting wicking behavior

To assess membrane quality and categorize membranes based on wicking speed, standardized wicking experiments were conducted. Membrane samples measuring 25 mm × 75 mm were clamped in a suspension device and immersed in a thin film of test liquid. Capillary forces drive liquid imbibition into the porous structure. The height h of the advancing liquid front was recorded over time t through imaging. A scheme of the setup is illustrated in Fig. 1. The time required to wet a distance of 40 mm was defined as the wicking time t_{w}, while the overall curve shape characterizes the wicking behavior.

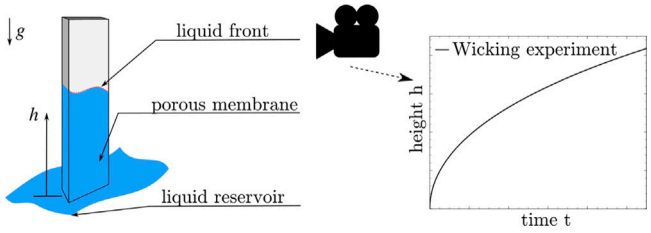

Fig. 1. Schematic representation of the observation process for liquid imbibition in a porous membrane, known as a wicking experiment (left), and the corresponding wicking curve obtained by tracking the liquid front over time (right).

3. Results

3.1. Determination of a directionally-dependent effective pore radius

To accurately represent the capillary pressure in porous structures, the determination of the effective pore radius r_{eff} from Eq. (11) is essential. An approach was developed that calculates the mean curvature H of the free interface Ω_{lg} in a fully resolved porous structures using two-phase phase-field simulations. From this, an effective pore radius r_{eff} is calculated, which describes the radius of a closed circular capillary with an equivalent mean curvature, with the following geometric coherency

$$r_{\text{eff}} = \frac{\cos\theta}{H}\,. \tag{23}$$

Thereby, the mean curvature H of the interface between the two phases liquid and air is based on the underlying phase field $\phi(\mathbf{x})$ and can be calculated with the simulation software PACE3D [27] due the following relation [10]

$$H = \frac{1}{N_I}\sum_{i=1}^{N_x}\sum_{j=1}^{N_y}\sum_{k=1}^{N_z}\frac{1}{2}\nabla\frac{\nabla\phi(\mathbf{x})}{|\nabla\phi(\mathbf{x})|} \qquad \text{with } \mathbf{x}\in\Omega_{lg}, \tag{24}$$

where the number of voxels N_I in the diffuse interface Ω_{lg} between the liquid and gas phase is considered. Since the curvature H is only evaluated within the interface region Ω_{lg}, where the phase field variable ϕ smoothly transitions between phases, its gradient $\nabla\phi$ is never exactly zero. This ensures that division by $|\nabla\phi(\mathbf{x})|$ remains well-defined. To determine the mean curvature H, the wetting of a porous structure from an infinite fluid reservoir is simulated. For this purpose, the two-phase Allen–Cahn phase-field model presented in Section 2.1.1 is applied with an energetic wetting boundary condition and without gravitational influence. Using a Neumann boundary condition with the normal derivatives of the order parameter $\partial\phi/\partial n = 0$ on the symmetry planes and an initial partial filling (see Fig. 2(a)), complete wetting of the considered structure in the observed wetting direction x can be mapped. The driving mechanism for wetting the structure is based on the minimization of the free surface in Eq. (3). Based on the simulation, the mean curvature $H_{x,i}$ of the free surface at each time step i is calculated by solving Eq. (24). As soon as the fluid has wetted 90% of the total structure length l_x after n time steps, an averaged mean curvature H_x is calculated

$$H_x = \frac{1}{n}\sum_{i=1}^{n}H_{x,i}, \tag{25}$$

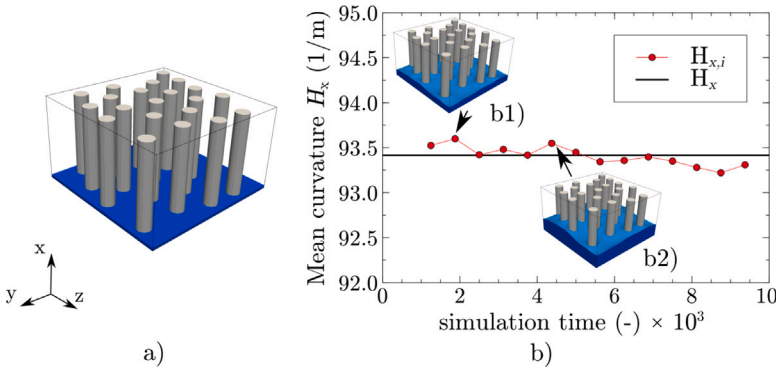

Fig. 2. Calculation of the effective pore radius $r_{\mathrm{eff},x}$ in x-direction. In Fig. (a) the initial partial filling for simulating the wetting of the fully resolved structure is shown, which is realized by means of a Neumann boundary condition. Fig. (b) exemplarily shows the measurement of the mean curvature $H_{x,i}$ of the free surface as well as the mean value of the curvature H_x determined according to Eq. (25). Furthermore, in (b1) and (b2) the free surface of the fluid is shown at two different time points.

Table 2
A complete list of simulation parameters employed in the validation study for the calculation of an effective pore radius.

Parameter	γ_{lg} (mN m^{-1})	θ (°)	Δt (µs)
Value	72	50	5.208

as exemplarily shown in Fig. 2(b). Finally, the directionally-dependent effective pore radius $r_{\mathrm{eff},x}$ can be determined using Eq. (23). By changing the boundary conditions, H_y and H_z and thus $r_{\mathrm{eff},y}$ and $r_{\mathrm{eff},z}$ can be further calculated.

3.2. Validation of directionally-dependent effective pore radius determination

This section focuses on validating the method described in the previous section for calculating a directionally-dependent pore radius.

3.2.1. In a simplified porous structure

As a first proof of concept, capillary rise was simulated in a simplified cylindrical geometry, as shown in Fig. 2(a), to validate the proposed method for determining a directionally-dependent effective pore radius r_{eff}. The simulation results were then compared to the analytical Jurin equation [14] for calculating the resulting equilibrium height h_{eq}, taking into account the gravitational acceleration g and the fluid density ρ, calculated as

$$h_{\mathrm{eq}} = \frac{2\gamma_{\mathrm{lg}}\cos(\theta)}{\rho g r_{\mathrm{eff},x}} \,. \tag{26}$$

The simulation domain has a size of 15 mm×26 mm×26 mm with a spatial resolution of Δx, Δy und Δz equals 50 µm/cell. The Neumann boundary condition $\partial\phi/\partial n = 0$ is defined in the x-direction, and periodic boundary conditions are defined on the remaining boundaries. All cylinders have the same diameter. In total, six structures are investigated, with the radius of the cylinders varying from 0.5 mm to 1.75 mm. For the validation study, a contact angle of $\theta = 50°$ was adopted based on the findings of Zhdanov et al. [32]. Table 2 presents all the relevant simulation parameters.

Fig. 3(a) shows the wetting in equilibrium state of a cylinder structure with a cylinder radius of 1.25 mm. The comparison of the analytical solution of the capillary rise h_{eq} calculated according to Eq. (26) and the simulated capillary rise h_{sim} is shown in Fig. 3(b). The necessary effective pore radius $r_{\mathrm{eff},x}$ for Eq. (26) is calculated using the procedure described in Section 3.1. The prediction and the simulation show good agreement with a maximum deviation of 5.7%.

3.2.2. Prediction of wicking behavior in PPMs

In the following, the experimental wicking results are compared to the model predictions based on Eq. (14) by applying the proposed method for determining a directionally-dependent effective pore radius r_{eff}. In total, three different membrane samples and their corresponding experimental data sets are used, thereby the digital twins of Sample A and B are based on computer tomography scans [8]. Each membrane will be compared with experimental wicking data in the lateral x-direction. The digital twin of sample C is based on CLSM. In order to validate the directionally-dependent characteristic of the method to extract an effective pore radius, experimental wicking experiments were obtained in both lateral directions x and y for sample C. *Porefil*® was used as the test liquid. Commonly employed for capillary flow porometry measurements [33], *Porefil*® is a perfluoroether with low surface energy of $\gamma_{\mathrm{lg}} = 16\,\mathrm{mN\,m^{-1}}$, a contact angle of zero between the liquid–air interface and the solid surface, a viscosity of $\eta = 2.2\,\mathrm{mPa\,s}$ and a density of $\rho = 1800\,\mathrm{kg\,m^{-3}}$. This combination results in slow wicking behavior, which is advantageous for detecting the liquid front and further dynamic changes of the contact angle and the surface energy during the wicking process can be neglected [8]. Consequently, *Porefil*® provides controlled conditions that allow the validation of the prediction of the wicking behavior.

Fig. 4 examines the wicking behavior along the x-direction for sample A and B. Thereby, Fig. 4(b) and (c) present both the experimentally determined results and various modeling approaches for the temporal evolution of the wicking behavior for sample A and B, respectively. In total, three experimentally determined wicking curves are available in [10] for sample A and B. However, since these show a very good agreement, only one experiment is displayed for better clarity. To illustrate the necessity of an effective pore radius for modeling the driving capillary force in Eq. (14), first of all, for sample A the wicking behavior was modeled with the mean geometric pore radius $r_{\mathrm{p}} = 1.73$ µm [10]. It is illustrated in Fig. 4(b), that the modeled wicking time is significantly underestimated, as the capillary force is significantly overestimated with the geometric pore radius. This can be attributed to the open-pored and highly porous nature of the membrane. Furthermore, the prediction of the wicking is modeled with an effective capillary radius of $r_{\mathrm{c}} = 1.73\,\mu\mathrm{m}$, based on the correction factor $F(r_{\mathrm{l}}, r_{\mathrm{p}})$ from Eq. (2) and a mean ligament radius of $r_{\mathrm{l}} = 0.72$ µm [10]. This approach, as already shown in [8], offers a very good agreement with the experimental values. However, a directionally-dependency of the capillary force cannot be mapped with the method by Altschuh et al. [8]. This anisotropic behavior can be considered with the approach presented in this work for calculating an effective pore radius r_{eff}. For sample A and B, the experimentally determined wicking profiles along the lateral x-direction agree convincingly with the macroscopic modeling approach based on Eq. (14) and the method for calculating an effective pore radius r_{eff}. Thereby, at a wicking distance of 40 mm, the relative deviation between the modeled and experimental wicking time

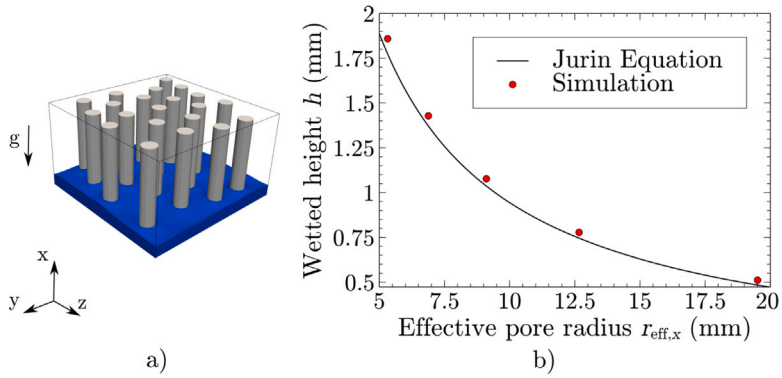

Fig. 3. Fig. (a) shows the simulated wetting in equilibrium state of a cylinder structure with a cylinder radius of 1.25 mm, considering the effect of gravity. In (b), the analytical capillary rise determined by the Jurin Eq. (26) is compared to the simulated capillary rise as a function of the effective pore radius $r_{\text{eff},x}$. The maximum deviation between the simulated and analytical solution is 5.7%.

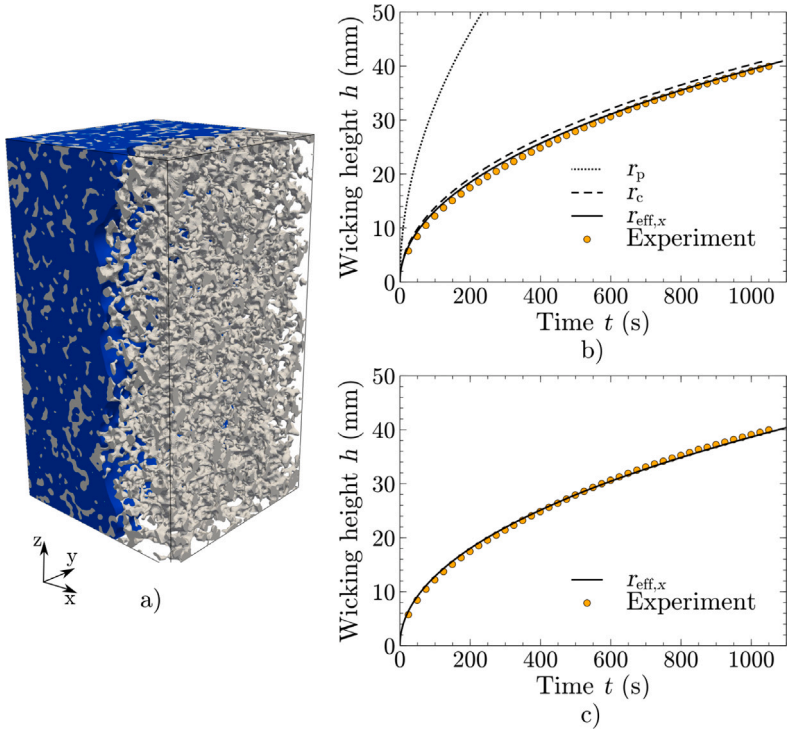

Fig. 4. Fig. (a) shows the fully resolved digital twin of the microstructure of Sample A during the two-phase wetting simulation, in order to extract an effective pore radius in x-direction. Fig. (b) shows the comparison of the wicking experiment and the different modeling approaches for predicting the wicking behavior of sample A. The capillary pressure was mapped considering the mean geometric pore radius r_p, the capillary radius r_c, and the approach presented in this work (see Section 3.1) for determining a directionally-dependent effective pore radius $r_{\text{eff},x}$. In (c) only the wicking prediction based on the effective pore radius for sample B is compared to the experimental results. For both Samples, *Porefil*® was used as the wicking fluid.

is −0,98% for sample A and 3,05% for sample B. It should be noted that the wicking prediction is based exclusively on effective structural parameters without any adjustment to experimental values.

To illustrate the potential for representing directional dependency, additional wicking experiments were conducted with a third sample C, in both, the lateral x- and y-direction. For each direction, three identical experiments according to the method described in Section 2.4 are carried out. An experimentally observed directionally-dependent wicking behavior can be seen in Fig. 5(a). The wicking time in the lateral y-direction is systematically longer compared to the x-direction. Since the three respective experiments in Fig. 5(a) yield consistent results, only one experiment is shown in the following for better overview.

Fig. 5(b) compares the experimental and modeled wicking behavior of sample C, based on its effective structural properties. The model incorporates the capillary effect described by Eq. (14), utilizing the directionally-dependent effective pore radius r_{eff} determined according to the method outlined in Section 3.1. Thereby, a very good agreement between the model and experiment for the wicking behavior can be observed. The deviations in lateral directions are well captured, with an overestimation of 3,7% in the x-direction and an underestimation of 6,1% in the y-direction at a wicking height of 39 mm. Due to temporary limitations in the automated tracking system, the wicking measurements were terminated at a height of 39 mm. Therefore, the reported wicking times correspond to this specific height. The fact that the anisotropic wicking behavior can be successfully modeled by the directionally-dependent structural parameters suggests that this observed structural anisotropy is responsible for the observed directionally-dependent wicking behavior.

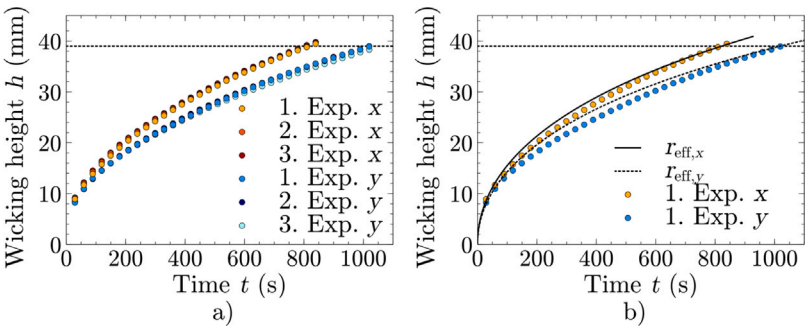

Fig. 5. Fig. (a) shows the wicking experiments for sample C in the lateral x- and y-directions. *Porefil*® was used as the wetting fluid. In Fig. (b), the modeled wicking behavior is compared to the experimental results. The modeling is based on the effective structural parameters of sample C extracted from the obtained digital twin.

3.3. Wetting properties

The interaction of a liquid with the intrinsic surface of a porous structure results in the formation of the contact angle θ. This angle is determined by Young's equation [34], which describes the balance of forces between the surface and interfacial tensions. Spontaneous wetting of the structure and the associated liquid flow occur when the contact angle lies within the range of $0° < \theta \leq 90°$. To counteract the hydrophobic properties of NC membranes and enable uniform wetting, the diagnostic membranes are treated with surfactant-based wetting agents [35,36]. As the surfactant concentration increases, the surface energy and contact angle decrease [37]. The treatment with surfactants can be achieved during the production process either by adding the wetting agent to the casting solution or by subsequent immersion in a wetting agent bath. The latter is referred to as impregnation, assuming that the surfactants are located on the intrinsic membrane surface.

When using water as the wicking fluid, interaction between the surfactants and the free surface must be expected during the wetting process. Due to their hydrophobic molecular part, the surfactants can enrich at the free liquid surface, which in turn leads to a variation of the surface energy and thus, contact angle properties. This process is referred to as dynamic modification of wetting properties and can also be induced by adding surfactants to the wicking fluid [10]. To investigate the influence of such a surfactant treatment on the imbibition process with water as wetting liquid, parametric studies were conducted using the NC membrane of sample C. The results of the computations prove the capability of the proposed method to calculate wetting properties, which would otherwise require costly experimental analysis.

3.3.1. Influence of impregnation process on wicking behavior

In [38], the influence of surfactant concentration on the wicking process with water is investigated by Starov et al. For porous NC membranes, it has been shown that below a critical pore radius, the capillary process remains unaffected by the addition of surfactants. Therefore, it is experimentally investigated for sample C whether this critical pore radius is not undercut and the surfactant addition has an influence on the wicking behavior. The wicking behavior in the x- and y-directions is investigated for this sample, both with and without impregnation of the intrinsic membrane surface. Distilled water with a surface energy of $\gamma_{\mathrm{lg}} = 72\,\mathrm{mN\,m^{-1}}$, a viscosity of $\eta = 1\,\mathrm{mPa\,s}$ and a density of $\rho = 998\,\mathrm{kg\,m^{-3}}$ was used as the wicking fluid. All wicking experiments were carried out according to the standardized wicking experiment described in Section 2.4, with each investigation consisting of three experimental runs.

Fig. 6(a) and (b) show the wicking profiles for membrane sample C without and with impregnation, respectively. It is clearly evident that the experiments are reproducible and that, as with the investigations using *Porefil*®, a slower wicking behavior occurs in y-direction compared to the x-direction both without and with impregnation. Furthermore, it is clear that impregnation accelerates the wicking behavior. For a wicking height of 40 mm, the average wicking time in the x-direction changes from 98.69(102) s to 71.93(107) s due to impregnation, and in the y-direction from 126.14(85) s to 96.64(214) s. Thus, it was experimentally proven that the critical pore radius is not undercut and that surfactant addition by impregnation has a significant influence on the wicking behavior.

3.3.2. Derive wetting properties

In the following investigations, the wicking behavior with impregnation will be examined in more detail, as this corresponds to the real-world application in lateral flow assays. A new approach is presented that allows for the determination of averaged wetting properties for the wicking behavior of water on a specific NC membrane type. The actually dynamic wetting process is simplified by assuming a constant average surface energy $\overline{\gamma}_{\mathrm{lg}}$ and a constant average contact angle $\overline{\theta}$.

To determine the averaged wetting properties of the membrane of sample C considering an impregnation, the experimentally determined wicking times in the x-direction $t_{\mathrm{W},x} = 71.93(107)\,\mathrm{s}$ and perpendicular in y-direction $t_{\mathrm{W},y} = 96.64(214)\,\mathrm{s}$ at a wicking height of 40 mm are used. Furthermore, the effective structural parameters from Table 1 and the macroscopic model from Eq. (14) are used. In this model, the wetting properties, surface energy γ_{lg} and contact angle θ, are defined as averaged variables, resulting in the time evolution function $t_{\mathrm{W}}(\overline{\gamma}_{\mathrm{lg}}, \overline{\theta})$. Thus, a relative deviation $\delta t_{\mathrm{W}}(\overline{\gamma}_{\mathrm{lg}}, \overline{\theta})$ of the projected wicking time $t_{\mathrm{W}}(\overline{\gamma}_{\mathrm{lg}}, \overline{\theta})$ and the experimentally determined wicking time t_{W} can be calculated as follows:

$$\delta t_{\mathrm{W}}(\overline{\gamma}_{\mathrm{lg}}, \overline{\theta}) = \frac{|t_{\mathrm{W}}(\overline{\gamma}_{\mathrm{lg}}, \overline{\theta}) - t_{\mathrm{W}}|}{t_{\mathrm{W}}} \cdot 100\%. \tag{27}$$

Fig. 7(a) shows this relative deviation for membrane sample C and the wicking behavior in the x-direction as a contour plot. The isolines display the possible combinations of average surface energy and contact angle with the corresponding relative deviation. The isoline where the projected wicking time matches the experimental one is highlighted in red. If the same procedure is now applied to the wicking behavior in y-direction, a combination of surface energy $\overline{\gamma}_{\mathrm{lg,min}}$ and contact angle $\overline{\theta}_{\mathrm{min}}$, can be found, where the total deviation in both the x- and y-directions is minimized

$$\min\left(\frac{|t_{\mathrm{W},x}(\overline{\gamma}_{\mathrm{lg}}, \overline{\theta}) - t_x|}{t_x} + \frac{|t_{\mathrm{W},y}(\overline{\gamma}_{\mathrm{lg}}, \overline{\theta}) - t_y|}{t_y}\right). \tag{28}$$

For the membrane of sample C, this procedure results in an averaged contact angle of $\overline{\theta}_{\mathrm{min}} = 19.3°$ and an averaged surface energy of $\overline{\gamma}_{\mathrm{lg,min}} = 64.5\,\mathrm{mN\,m^{-1}}$. Fig. 7(b) compares the projected wicking behavior both in the x- and y-direction with the experimental data with distilled water as wicking fluid. The results show good agreement, considering the obtained average contact angle $\overline{\theta}$ and surface energy $\overline{\gamma}_{\mathrm{lg}}$.

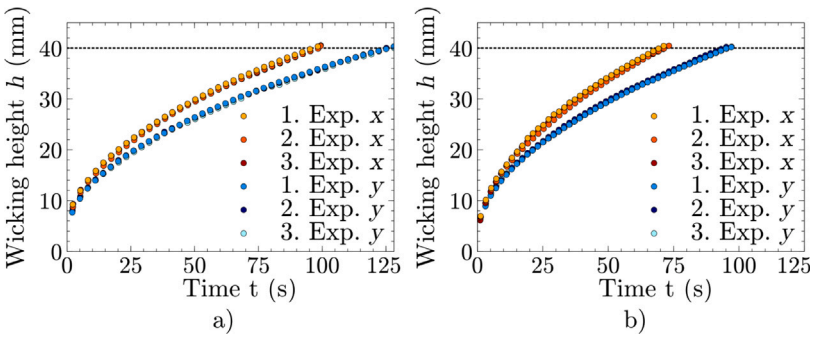

Fig. 6. In Fig. (a), the wicking experiments for sample C are shown in the lateral x- and y-directions without an impregnation. In Fig. (b), the same investigations were carried out, whereby the membrane sample was impregnated with surfactants on the intrinsic membrane surface. For all experiments, distilled water was used as the wicking liquid.

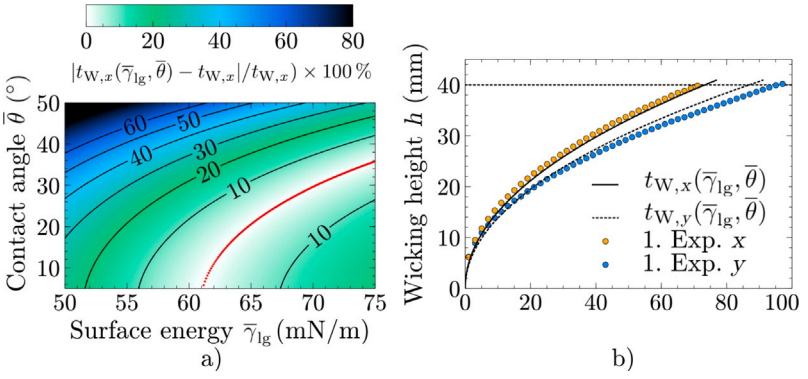

Fig. 7. In Fig. (a), the relative deviation $\delta t_{W,x}(\overline{\gamma}_{lg},\overline{\theta})$ between the projected wicking time $t_{W,x}(\overline{\gamma}_{lg},\overline{\theta})$ and the experimentally determined wicking time $t_{W,x}$ in the x-direction is presented as a contour plot for sample C, depending on the contact angle $\overline{\theta}$ and the surface energy $\overline{\gamma}_{lg}$, as described by Eq. (27). Fig. (b) illustrates the comparison between the experimental and predicted wicking behavior in x- and y-direction for sample C, using the wetting properties $\overline{\theta}$ and $\overline{\gamma}_{lg}$, which are determined using Eq. (28).

4. Discussion

This study presents a novel methodology for determining a directionally-dependent effective pore radius in porous membranes, enabling accurate prediction of the capillary driven wicking behavior in lateral flow assays. By employing 3D digital twins created from high-resolution imaging techniques like confocal laser scanning microscopy and computed tomography, effective structural properties of nitrocellulose membranes were examined at the pore scale. Thereby, the effective pore radius is determined by simulating a two-phase imbibition process within the pore space of the digital twin, utilizing a phase-field approach. By changing the initial partial filling, an effective pore radius in each lateral direction can be determined. Subsequently, a macroscopic wicking model based on a Darcy approach was employed, integrating the effective properties to predict wicking behavior on an application scale. The validation of the prediction with experimental data indicates that the introduced effective pore radius significantly enhances the modeling of capillary-driven wicking compared to using the geometric pore radius. Furthermore, compared to the state of the art [8], it improves the ability to capture the directional dependency of porous structures. The study validates the robustness of the method by achieving close agreement between predicted and experimental wicking behavior, with deviations below 6% across multiple samples. The proposed method highlights the importance of incorporating directional anisotropy when modeling wicking behavior, as evidenced by the differences in experimental wicking times observed in lateral directions. This finding is critical for optimizing LFA membrane designs, where precise control over liquid flow is essential.

The presented approach can further be used to assess wetting properties such as the average contact angle and surface energy, showcasing its versatility and potential to lessen reliance on costly experimental techniques. By employing computational methods, the research quantifies the influence of individual material parameters on the wicking process, provides insight into the underlying physical mechanisms, and contributes to the design of more efficient and reliable LFAs, while addressing key challenges in the characterization of porous materials.

5. Conclusion

This study successfully introduces a computational framework for the accurate prediction of wicking behavior in open-pored porous membranes, with specific focus on porous polymeric membranes, used for LFAs. By employing 3D digital twins derived from advanced imaging techniques, the method enables the determination of a directionally-dependent effective pore radius, a parameter critical for modeling capillary-driven fluid flow in complex porous structures. The proposed approach overcomes the limitations of current capillary pore radius-based models by incorporating structural anisotropy, resulting in highly accurate predictions of wicking behavior. The successful validation of the methodology, evidenced by its accurate prediction of wicking behavior across various porous membrane samples and its ability to extract wetting properties such as contact angle and surface energy, underscores its robustness and broad applicability. This computational approach not only reduces the reliance on costly and time-consuming experimental analyses but also provides a deeper understanding of the relationship between pore-scale structure and macroscopic fluid dynamics. The results pave the way for improved membrane design and selection in LFAs, ensuring more efficient and reliable performance. Furthermore, the presented characterization method has potential applications in other fields where porous materials play a key role, such as filtration, catalysis, and tissue engineering.

CRediT authorship contribution statement

Willfried Kunz: Writing – original draft, Visualization, Validation, Software, Methodology, Formal analysis, Conceptualization. **Alexander Spreinat:** Writing – review & editing, Data curation, Conceptualization. **Christian H. Maack:** Data curation. **Andrea Ernst:** Supervision, Data curation. **Jennifer Niessner:** Writing – review & editing, Supervision. **Britta Nestler:** Writing – review & editing, Supervision, Funding acquisition.

Declaration of Generative AI and AI-assisted technologies in the writing process

During the preparation of this work, the authors used ChatGPT to improve readability and language of the work. After utilizing this tool, the authors reviewed and edited the content as needed and take full responsibility for the publication's content.

Declaration of competing interest

The authors declare that they have no known competing financial interests or personal relationships that could have appeared to influence the work reported in this paper.

Acknowledgments

This work was mainly supported by the German government, through the BMBF project Multipore (project ID: 13FH020KX0) and by Sartorius Stedim Biotech GmbH in Goettingen, Germany. Britta Nestler further acknowledges the support of the Helmholtz Association, Germany within the MSE program, no. 43.31.01.

Data availability

The authors do not have permission to share data.

References

[1] E. Kissa, Wetting and wicking, Text. Res. J. 66 (10) (1996) 660–668.
[2] D. Gasperino, T. Baughman, H.V. Hsieh, D. Bell, B.H. Weigl, Improving lateral flow assay performance using computational modeling, Annu. Rev. Anal. Chem. 11 (2018) 219–244, http://dx.doi.org/10.1146/annurev-anchem-061417-125737.
[3] R. Masoodi, K.M. Pillai, Wicking in Porous Materials: Traditional and Modern Modeling Approaches, CRC Press, Boca Raton, FL, 2012.
[4] N. Fries, D. Quéré, Capillary Transport Processes in Porous Materials-Experiment and Model, Cuvillier Verlag, Göttingen, GER, 2010.
[5] R. Masoodi, K.M. Pillai, P.P. Varanasi, Darcy's law-based models for liquid absorption in polymer wicks, AIChE J. 53 (11) (2007) 2769–2782.
[6] A. Boţan, F.-J. Ulm, R.J.-M. Pellenq, B. Coasne, Bottom-up model of adsorption and transport in multiscale porous media, Phys. Rev. E 91 (3) (2015) 032133.
[7] F. Jamshidi, W. Kunz, P. Altschuh, M. Bremerich, R. Przybylla, M. Selzer, B. Nestler, Geometric flow control in lateral flow assays: Macroscopic single-phase modeling, Phys. Fluids 34 (2022) 062110, http://dx.doi.org/10.1063/5.0093316.
[8] P. Altschuh, W. Kunz, M. Bremerich, A. Reiter, M. Selzer, B. Nestler, Wicking in porous polymeric membranes: Determination of an effective capillary radius to predict the flow behavior in lateral flow assays, Membranes 12 (7) (2022) http://dx.doi.org/10.3390/membranes12070638.
[9] T. Bultreys, W. De Boever, V. Cnudde, Imaging and image-based fluid transport modeling at the pore scale in geological materials: A practical introduction to the current state-of-the-art, Earth-Sci. Rev. 155 (2016) 93–128.
[10] P. Altschuh, Skalenübergreifende Analyse Makroporöser Membranen im Kontext Digitaler Zwillinge (Dissertation), Karlsruhe Institute of Technology, Karlsruhe, 2020, http://dx.doi.org/10.5445/IR/1000122904.
[11] A. Ley, P. Altschuh, V. Thom, M. Selzer, B. Nestler, P. Vana, Characterization of a macro porous polymer membrane at micron-scale by Confocal-Laser-Scanning Microscopy and 3D image analysis, J. Membr. Sci. 564 (2018) 543–551, http://dx.doi.org/10.1016/j.memsci.2018.07.062.
[12] W. Kunz, Datengetriebene Analyse der Strukturabhängigen Flüssigkeitsausbreitung in Porösen Membranen (Dissertation), Karlsruhe Institute of Technology, Karlsruhe, 2024, http://dx.doi.org/10.5445/IR/1000175158.
[13] M.V. Berry, The molecular mechanism of surface tension, Phys. Educ. 6 (2) (1971) 79.
[14] P.-G. Gennes, F. Brochard-Wyart, D. Quéré, et al., Capillarity and Wetting Phenomena: Drops, Bubbles, Pearls, Waves, Springer, 2004.
[15] R. Masoodi, K.M. Pillai, P.P. Varanasi, Role of hydraulic and capillary radii in improving the effectiveness of capillary model in wicking, in: Fluids Engineering Division Summer Meeting, Vol. 48401, 2008, pp. 251–259.
[16] S. Ravi, R. Dharmarajan, S. Moghaddam, Measurement of capillary radius and contact angle within porous media, Langmuir 31 (47) (2015) 12954–12959, http://dx.doi.org/10.1021/acs.langmuir.5b03113.
[17] M. Sophocleous, Understanding and explaining surface tension and capillarity: an introduction to fundamental physics for water professionals, Hydrogeol. J. 18 (4) (2010) 811.
[18] B. Nestler, F. Wendler, M. Selzer, B. Stinner, H. Garcke, Phase-field model for multiphase systems with preserved volume fractions, Phys. Rev. E—Stat. Nonlinear Soft Matter Phys. 78 (1) (2008) 011604.
[19] H. Garcke, B. Nestler, B. Stinner, F. Wendler, Allen–Cahn systems with volume constraints, Math. Models Methods Appl. Sci. 18 (08) (2008) 1347–1381.
[20] M. Ben Said, M. Selzer, B. Nestler, D. Braun, C. Greiner, H. Garcke, A phase-field approach for wetting phenomena of multiphase droplets on solid surfaces, Langmuir 30 (14) (2014) 4033–4039, http://dx.doi.org/10.1021/la500312q.
[21] N. Fries, M. Dreyer, An analytic solution of capillary rise restrained by gravity, J. Colloid Interface Sci. 320 (1) (2008) 259–263.
[22] G. Løvoll, Y. Méheust, K.J. Måløy, E. Aker, J. Schmittbuhl, Competition of gravity, capillary and viscous forces during drainage in a two-dimensional porous medium, a pore scale study, Energy 30 (6) (2005) 861–872.
[23] C. Byon, S.J. Kim, The effect of meniscus on the permeability of micro-post arrays, J. Micromech. Microeng. 21 (11) (2011) 115011.
[24] J. Cai, E. Perfect, C.-L. Cheng, X. Hu, Generalized modeling of spontaneous imbibition based on Hagen–Poiseuille flow in tortuous capillaries with variably shaped apertures, Langmuir 30 (18) (2014) 5142–5151.
[25] N. Otsu, A threshold selection method from gray-level histograms, IEEE Trans. Syst. Man Cybern. 9 (1) (1979) 62–66.
[26] L.-K. Huang, M.-J.J. Wang, Image thresholding by minimizing the measures of fuzziness, Pattern Recognit. 28 (1) (1995) 41–51.
[27] J. Hötzer, A. Reiter, H. Hierl, P. Steinmetz, M. Selzer, B. Nestler, The parallel multi-physics phase-field framework Pace3D, J. Comput. Sci. 26 (2018) 1–12, http://dx.doi.org/10.1016/j.jocs.2018.02.011.
[28] J. Joos, T. Carraro, A. Weber, E. Ivers-Tiffée, Reconstruction of porous electrodes by FIB/SEM for detailed microstructure modeling, J. Power Sources 196 (17) (2011) 7302–7307.
[29] P.W. Hoffrogge, D. Schneider, F. Wankmüller, M. Meffert, D. Gerthsen, A. Weber, B. Nestler, M. Wieler, Performance estimation by multiphase-field simulations and transmission-line modeling of nickel coarsening in FIB-SEM reconstructed Ni-YSZ SOFC anodes I: Influence of wetting angle, J. Power Sources 570 (2023) 233031.
[30] A.C. Liakopoulos, Darcy's coefficient of permeability as symmetric tensor of second rank, Hydrol. Sci. J. 10 (3) (1965) 41–48.
[31] W. Kunz, P. Altschuh, M. Bremerich, M. Selzer, B. Nestler, Source Data Belonged to "Establishing Structure-Property Linkages for Wicking Time Predictions in Porous Polymeric Membranes Using a Data-Driven Approach", Zenodo, 2022, http://dx.doi.org/10.5281/zenodo.7220573.
[32] S. Zhdanov, V. Starov, V. Sobolev, M. Velarde, Spreading of aqueous SDS solutions over nitrocellulose membranes, J. Colloid Interface Sci. 264 (2) (2003) 481–489.
[33] M.R. Mohd Ramli, A.L. Ahmad, C.P. Leo, Surface modification of polytetrafluoroethylene hollow fiber membrane for direct contact membrane distillation through low-density polyethylene solution coating, ACS Omega 6 (7) (2021) 4609–4618.
[34] T. Young, III. An essay on the cohesion of fluids, Philos. Trans. R. Soc. Lond. (95) (1805) 65–87.
[35] M.A. Mansfield, The use of nitrocellulose membranes in lateral-flow assays, in: Drugs of Abuse: Body Fluid Testing, Springer, 2005, pp. 71–85.
[36] M.A. Mansfield, Nitrocellulose membranes for lateral flow immunoassays: a technical treatise, Lateral Flow Immunoass. (2009) 1–19.
[37] K. Lee, N. Ivanova, V. Starov, N. Hilal, V. Dutschk, Kinetics of wetting and spreading by aqueous surfactant solutions, Adv. Colloid Interface Sci. 144 (1–2) (2008) 54–65.
[38] V. Starov, S. Zhdanov, M. Velarde, Capillary imbibition of surfactant solutions in porous media and thin capillaries: partial wetting case, J. Colloid Interface Sci. 273 (2) (2004) 589–595.